Applications of Small Angle Neutron Scattering in Material Science and Technology

F. RUSTICHELLI - Istituto di Scienze Fisiche - Università degli Studi di Ancona, Italy

Abstract

A review is presented of applications of Small Angle Neutron Scattering technique in material science and technology. The essential theoretical bases of the technique are reported. Then a brief description of the experimental facilities in given. Finally several applications of the technique to inorganic materials are considered. In particular the paper reports investigations concerning materials for aeronautical technology, for electric power plants, for thermonuclear fusion reactor technology and for electronics. Then reference is made to investigations of glasses, high Tc superconductors, ceramics, catalysts, fibres, composite materials, cement clay and porous rocks, and nanocrystals.

Riassunto

Viene presentata una rivista delle applicazioni della tecnica di Diffusione dei Neutroni a Basso Angolo. Sono riportate le basi teoriche essenziali della tecnica. Quindi viene data una breve descrizione dei dispositivi sperimentali. Infine vengono prese in considerazione diverse applicazioni della tecnica all'indagine di materiali inorganici. In particolare il lavoro riporta degli studi riguardanti i materiali per la tecnologia aeronautica, per gli impianti di produzioni di energia elettrica, per la tecnologia dei reattori a fusione termonucleare e per l'elettronica. Quindi si fa riferimento a studi sui vetri, vetri metallici, superconduttori ad alta temperatura, ceramici, catalizzatori, cementi argille e rocce porose, e nanocristalli.

Introduction

Neutron techniques are undergoing in recent times the same development as some decades ago X-ray techniques have done, namely they are not only used to solve physical problems, but they are more and more used by chemists, biologists, geologists, material scientists and engineers, in particular in connection with the development of modern and very intense neutron sources.

The applications of neutrons to material science and technology are very broad and the reader should refer to [1] for a complete and detailed overview. Essentially all the neutron techniques are non destructive, due to the large penetration of neutrons. In particular structural investigations can be carried out by Small Angle Neutron Scattering (SANS), residual stress determination by Neutron Diffraction and surface and interfaces investigations by Specular Neutron Reflection. Moreover Neutron Diffraction can be used to determine textures and crystallographic structures, whereas neutron radiography can provide useful informations complementary to X-ray radiography. In this paper the capibilities offered by SANS in materials science and technology will be considered.

Small angle neutron scattering (SANS) is a technique which is able to deliver microstructural information, in a non destructive way, on inhomogeneities present in materials, in the size range between the nanometer and the micrometer. As a consequence it is complementary to the more usual transmission electron microscopy (TEM) technique. In fact SANS provide information which is averaged over a volume ranging from one cubic millimeter to several cubic centimeters, whereas TEM provide a detailed information over a very localized area, so that the total volume of samples analyzed until now in overall the world by TEM is of the same order of magnitude of one single sample for SANS.

Moreover the theory of SANS is very similar to the theory of small angle x-ray scattering (SAXS) technique, which was previously developed, and which is still the most common one, but suffers, in spite of the availability of the very strong x-ray sources, like synchrotron radiation facilities, of the severe limitation consisting in the very reduced penetration depth of this kind of radiation (few hundreth μm). The next section will be devoided to recall some basic principles of the theory of SANS, then the experimental techniques will be presented and finally several applications of SANS related to modern materials science and technology will be considered.

Theoretical bases

General concepts

A schematic representation of the coherent elastic scattering process in the real space and the reciprocal space is reported in Fig. 1a. The incident neutrons have a momentum $\underline{P}_0 = \hbar\,\underline{K}_0$, while the scattered neutrons have a momentum $\underline{P}_1 = \hbar\,\underline{K}_1$, where $K_0 = K_1 = 2\pi/\lambda$, being λ the neutron wavelength. The momentum transfer occurring during the scattering event is $\underline{P}_1 - \underline{P}_0 = \hbar\,(\underline{K}_1 - \underline{K}_0) = \hbar\underline{Q}$. The quantity $|Q|$ is equal to $(4\pi/\lambda)$, sin θ.

For small angle scattering, the measured scattered intensity at a given scattering vector $\underline{Q}$ is proportional to the macroscopic scattering cross section $d\Sigma/d\Omega(\underline{Q})$ (which refes to the unit volume and can be expressed in cm^{-1}) given by the expression

$$\frac{d\Sigma}{d\Omega}(\underline{Q}) = \frac{1}{V}\left|\int_V \varrho(\underline{r})\, e^{i\underline{Q}\cdot\underline{r}}\, d^3\,\underline{r}\right|^2 \tag{1}$$

where the integration is over the entire specimen volume, V, illuminated by the primary neutron beam, and $\varrho(\underline{r})$ is the neutron coherent scattering lenght density, which contains structural information for the sample and is defined as

$$\varrho(\underline{r}) = \Sigma\; n_i\; b_i \tag{2}$$

n_i being the number of nuclei of type i contained in the unit volume around $\underline{r}$ and b_i the corresponding neutron coherent scattering length, which is known for each nucleus [2].

The integral appearing in eq. (1) is the amplitude of the scattered wave, where contributions from the different scattering centers are multiplied by the phase factors $e^{i\underline{Q}\cdot\underline{r}}$ which are related to the interference phenomenon.

The most general problem in neutron scattering is to use the eq. (1) in order to extract from the measured scattering cross section $d\Sigma/d\Omega(\underline{Q})$ the unknown function $\varrho(\underline{r})$ which provides the structure of the sample. That means one must solve the integral equation expressed by eq. (1), which is in general not so easy to do.

However we will consider some special cases which are very important from practical point of view and which imply relatively simple mathematical treatments of the data. For a more complete theoretical treatment of the small angle scattering technique one should refer to [3-11], including textbooks or review articles.

The two-phase model

The case will be considered here of distinct particles (precipitates, voids, gas bubbles, second phases) of identical shape, randomly dispersed in a matrix and sufficiently dilute so that interparticle interference effects can be neglected.

In this case it can be shown that eq. (1) becomes

$$\frac{d\Sigma}{d\Omega}(\underline{Q}) = \frac{V_p^2\; N_p}{V}(\Delta\varrho)^2 |F_p\;(\underline{Q})|^2 \tag{3}$$

where $\Delta\varrho$, the neutron contrast, is defined as:

$$\Delta\varrho = \varrho_m - \varrho_p \tag{4}$$

being ϱ_m and ϱ_p the neutron coherent scattering length densities of the matrix and of the particle, respectively, and N_p the total number of particles contained in the specimen.

The function $F_p(\underline{Q})$ is the single-particle form factor defined by

$$F_p(\underline{Q}) = \frac{1}{V_p} \int_{V_p} e^{i\underline{Q}\cdot\underline{r}} \, d^3\underline{r} \tag{5}$$

where V_p is the volume of the particle.

For a sphere of radius R the scattering function $S(Q) = |F_p(Q)|^2$ is given by

$$S(Q) = \{3[\sin(QR) - QR\cos(QR)] / Q^3 R^3\}^2 \tag{6}$$

which is a function of QR.

The function (6) is represented in Fig. 1b and shows quite well the inversion relation between reciprocal space (Q measured in nm^{-1}) and the real space (R measured in nm): large (small) particles produce scattering at small (large) values of Q, i.e. to small (large) angles.

Structural quantities obtainable by SANS

Number of particles per unit volume

As, according to (5), $F_p(0) = 1$, by extrapolating to zero the experimental values of the scattering cross section $d\Sigma/d\Omega(\underline{Q})$ one obtains, according to eq. 3,

$$\frac{d\Sigma}{d\Omega}(\underline{Q}) = \frac{V_p^2 N_p}{V}(\Delta\varrho)^2, \tag{7}$$

so that by knowing the neutron contrast $\Delta\varrho$, which is easy to evaluate once the chemical compositions of the matrix and particles are known, and by knowing the volume V_p of each particle, which, in the case of spherical particles can be evaluated by the radius R obtained by the Guinier method of low Q approximation (see section 2.3.2.) one obtains the number of particles per unit volume N_p.

Gyration radius (Guinier Approximation)

For randomly oriented, sharp-edged scatterers of any given geometry, Guinier [4] has shown that at small values of QR, where R is a linear dimension of the particles, the scattering cross section $d\Sigma/d\Omega(\underline{Q})$ can be approximated by

$$\frac{d\Sigma}{d\Omega}(\underline{Q}) = \frac{V_p^2 N_p (\Delta\varrho)^2}{V} \exp(-R_g^2 Q^2/3) \tag{8}$$

where R_g, the gyration radius, is defined by

$$R_g^2 = \frac{1}{V_p} \int_{V_p} r^2 \, d^3\underline{r} \tag{9}$$

r being the distance of the volume element $d^3\underline{r}$ from the center of mass of the particle. For spheres of radius R one obtains $R_g = (3/5)^{1/2} R$.

The Guinier approximation is valid for $QR_g < 1.2$, and was largely used for monodisperse systems.

Specific surface (Porod Approximation)

For homogeneous particles whith sharp boundaries Porod [12] has shown that, for large Q, the following approximation is valid

$$\frac{d\Sigma}{d\Omega}(\underline{Q}) = \frac{2\pi(\Delta\varrho)^2\ S_p}{Q^4} \tag{10}$$

where the specific surface $S_p = S/V$ is the total surface area of the particles contained in the unit volume (S is the total surface of the particles contained in the volume V). By knowing the contrast $\Delta\varrho$ the specific surface S_p can be obtained from the asymptotic hehaviour

$$\lim_{Q\to\infty}\left[Q^4\ \frac{d\Sigma}{d\Omega}(\underline{Q})\right]$$

Volume fraction

It can be shown that by evaluating the integral in the Q space of the experimental scattering cross section

$$\widetilde{Q}\ (0) = \int \frac{d\Sigma}{d\Omega}(\underline{Q})\ d^3\ \underline{Q} \tag{11}$$

in the two phase model one can derive the volume fraction of the particles $C_p = (N_p\ V_p)/V$ from the equation

$$\widetilde{Q}\ (0) = (2\pi)^3\ C_p\ (1 - C_p)\ (\Delta\varrho)^2. \tag{12}$$

Size distribution for polydispersed systems

For a dilute system of particles having a size distribution n(R) defined as the number of particles per unit volume having linear dimensions between R and R + dR, it is easy to show that eq. (3) should be replaced, in the two phase model, by

$$\frac{d\Sigma}{d\Omega}(\underline{Q}) = \Delta\varrho\int_0^\infty n(R)\ V_p\ (R)\overline{|F_p\ (Q,\ R)|^2}\ dR \tag{13}$$

where $V_p(R)$ is the volume of a particle having linear dimension R and the bar indicates orientation averaging. It appears that in order to obtain from the measured $d\Sigma/d\Omega(\underline{Q})$ the unknown function n(R), from which many of the above mentioned structural quantities can be indipendently derived, one must solve the integral equation (13), once the shape of the particles is known or assumed and therefore also the form factor $|F_p\ (Q,\ R)|^2$ is known.

Several direct transformation methods where developed. A relatively recent general analytical method was developed by Fedorova and Schmidt [13], to which the reader should refer for previous works. In all these methods the solution n(R) is very sensitive to the extrapolated parts at low and large Q of the experimental scattering cross section. From a mathematical point of view, it is more easy to calculate the scattering cross section from a given model and adjusting eventually some parameters.

A more recent way consists [14] in approximating the unknown function n(R) with a linear combination of cubic spline functions Φ_k

$$n(R) = \sum_{K=1}^{N_k} C_k \, \Phi_k \, (z) \tag{14}$$

with $z = \ln R$.

The coefficients C_k are determined by a least-square fit of the measured $d\Sigma/d\Omega(Q)$.

Pair correlation function in presence of interference

When the number of particles is very high and interparticle interference effects occur, the scattering cross section can be approximated as the product of an intraparticle structure factor P(Q) and an average interparticle structure factor S(Q) describing the interference

$$\frac{d\Sigma}{d\Omega}(Q) = P\,(Q) \cdot S\,(Q) \tag{15}$$

The Fourier transform of S(Q) is the pair correlation function $g_c(r)$, which is the propability to find the center of mass of a particle at a distance r when another particle is at the origin.

A recent example of this type of problem is reported in ref. (15) and will be discussed below.

Special cases

A statistical dislocation arrangement produces a scattering cross section proportional to Q^{-3}.

For more detailed information as well as for the case of multiple refraction, characteristic length, surface effects, compositional fluctuations, magnetic scattering and critical scattering, the reader should refer for istance to [7].

Experimental facilities

Conventional point geometry facilities

The most powerful conventional facility is the D11 diffractometer installed at the High Flux Reactor at ILL Grenoble [16] which is represented schematically in Fig. 2. Its long flight path allows exploration of Q values as small as 10^{-3} nm^{-1}. The velocity selector produces monochromatic beams of wavelength $\lambda \approx 1$ nm, which avoids the double Bragg diffraction normally present in X-ray diffraction. The multidetector consists of 64×64 pixels and allows to record simultaneously the small angle scattering pattern.

Double crystal facilities

Very high resolution, i.e. very low values of Q ($Q = 10^{-5}$ nm^{-1}) can be obtained by using double crystal diffractometers. With such an instrument one can investigate particles of the order of few μm. The working principle is reported in Fig. 3.

In absence of the sample, diffraction from the second crystal occurs only when it is parallel to the first

one inside few seconds of arcs (width of the rocking curve). If now the sample is located between the two crystals, in order that neutrons which are scattered from the sample at an angle 2θ be diffracted from the second crystal and detected, the second crystal must be rotated by an angle 2θ, in order that the Bragg law be satisfied.

In practice a narrow rocking curve of the second crystal is recorded without sample and a broadened one with sample, from which the scattering cross section can be derived. Ref. 17, which should be considered for theoretical details, describes an instrument of this type using bent crystals in order to improve the intensity with a consequent loss of resolution.

Applications to inorganic materials

General considerations

Only some applications of SANS to inorganic materials will be considered here, by remembering that numerous applications of SANS exist to polymer science, micellar systems, liquid dispersions, gels and biomolecules. Moreover for each class of materials here considered a methodological approach will be followed i.e. more than a complete review of the results obtained in the past, only few (sometimes one) representative examples will be reported in order that the reader can have an idea of what can be done in the future by using SANS. Finally for each example, due to space limitations, the reader will find mainly the final physical results, and should refer to the original papers for details concerning the data treatments.

Aeronautical technology materials

A pioneer work on application of SANS to problems interesting applied technological research was performed by Pizzi and Walther [6], who in particular investigated the evolution of $\gamma' - Ni_3(Al, Ti)$ in a INCONEL-700 turbine blade for aircraft [18]. Fig. 4 reports the spatial dependence of the average radius of γ' precipitates along the axis of a blade operated at normal temperature after different operation times and of another one operated at higher temperature. The radius is maximum in the middle of the blades is higher for the second blade. We have here an example of how SANS could be used to determine the residual life of industrial components.

Binary Al-Li alloys are interesting as models for commercial alloys used in aeronautical applications and other technological fields. A recent experiment [15] was performed by SANS on the late stage of δ' (metastable phase of stoichiometric composition Al_3Li) precipitation in a high-purity Al-Li (3 wt. %) alloy aged at 463 K for different times, ranging between 1h and 90h. Some of the obtained results will be presented here of this emblematic experiment, characterized by polydispersity and interpaticle interference.

Fig. 5 report the obtained SANS cross section for some ageing times. Some qualitative information can be obtained. The observation of interference peaks indicates the presence of spatial correlation between the precipitates. The shift to lower Q values for higher aging times, indicates an increase of the interparticle distance, as can be deduced by the Bragg law considered as a very rough approximation for this non ordered system. The increase of the slope for higher ageing times, indicates an increase of the average precipitates radius, as deduced in a very rough way by the Guiner approximation (see section 2.3.2).

Quantitative results are reported in Fig.s 6-8. Fig. 6 shows the size distributions as obtained by the method using the spline function combination (eq. 14). An increase of the average size and a reduction of

the number of precipitates is observed for increasing ageing times. That is in agreement with the fact that the volume fraction remains constant [15]. Fig. 7 presents the cube of the average radius of precipitates as a function of the aging time. The Ostwald law, based on a diffusion-controlled coarsening model foreseeing a $t^{1/3}$ dependence of the average radius of the precipitates, appears to be verified inside the experimental errors.

Fig. 8 presents the effective reduced pair correlation function $g_e(r)$, obtained according to the method explained in sect. 2.3.6. The distance of a given peak from the origin represents the interprecipitate distance, which appears to increase for increasing ageing times. A dynamical scaling behaviour was observed for ageing times larger than 24 h, i.e. the scaled structure functions follow a universal curve [15]. In conclusion, as far as the ageing time increases, the volume fraction remains constant, the average radii of the precipitate increase, their mutual distance increases, the specific surface decreases and their number decreases.

A very recent SANS experiment was performed on single crystals of nickel based AM1 superalloy [19], owing to the technological interest of superalloy single-crystal turbine blades, which exhibit improved creep and fatigue properties as compared to the traditional polycristalline ones. In particular the evolution of morphology of γ' precipitates, which hinder the gliding of dislocations was investigated as a function of heat treatments and creep.

Fig. 9 reports SANS data for samples submitted to different thermo-mechanical treatments. In (a) the sample was annealed for 2 hours at 1050 °C and the <001> axis was parallel to the direction of the neutron beam. A fourfold symmetry is observed indicating a strong anysotropy along the crystallographic directions of the sample in the shape and arrangement of precipitates. In particular four interference peaks are observed along the <100> and <010> axes of the reciprocal space, indicating a regular arrangement of the precipitates on the nodes of a simple cubic "superlattice" of parameter L, parallel to the f.c.c. lattice of the single crystal.

The parameter L, which represents on one side the distance between adjacent γ' precipitates, and on the other hand the linear dimensions of the closed-packed cuboidal precipitates itself, as observed by electron mycroscopy, was deduced from the interference peaks by using the Bragg law. Fig. 9b reports the observed dependence of the volume L^3 on the annealing time at 1050 °C, which, except for small deviations at short annealing times, agrees with the Ostwald law, as it was the case for the data of Fig. 7 for Al-Li.

Fig. 9c refers to a sample submitted to a chemical Onera heat treatment and then to a creep test at 950 °C with a tensile stress of 280 MPa and an elongation of 1.5%. The observed elongated SANS pattern indicates the transformation of the precipitates from cuboidal to platelet shape, according to a peculiar coarsening mechanism induced by creep. SANS could allow in the future to observe "in situ" the kinetics of this transformation.

Electric power plants materials

General considerations

A very recent review of the SANS work performed on materials used in electric power plants can be found in ref. [20], together with a discussion of the interest of structural information for safety efficiency and reliability of the plant itself. Here only few representative results will be presented. The interest of SANS, as compared to TEM (which should be used anyway in basic investigations) is its non destructive character.

Turbine blades

A typical material employed in turbine blades for turbogas power plants is the Ni-based superalloy UDIMET 720, which presents a relatively high creep resistance at the operation temperatures reaching also 900 °C. Fig. 10 presents the γ' precipitate size distributions obtained by SANS for nontreated material and in a turbine blade before operation and after 8000 h operation at 800 °C. The turbine preparation treatment seems to increase the concentration of the bigger particles, whereas the operation of the turbine seems to induce the production of small precipitates and to increase the size of the other ones. For the other obtained structural information like volume fractions and correlation length, and for more details the reader should refer to [21-23].

Very recently SANS was used to characterize [52] the microstructural changes induced by the thermomechanical treatments used for the production of a turbine blade consisting of Ni-based superalloy IN 738.

Aisi 304 stainless steel

a) Carbide precipitation

Carbide (M_{23} C_6 where M is for metal) precipitation in austenitic stainless steels is associated to depletion of Cr in the matrix as a consequence of diffusion to the precipitates itself.

Several AISI 304 samples annealed at different temperatures for different times were investigated by SANS [24]. Fig. 11 reports the bimodal size distribution of the precipitates of intergranular and intragranular nature, which was obtained by SANS for a sample aged at 700 °C for 60 days and which appears in good ageement with TEM observation.

b) Creep microcavities

An attempt to characterize by SANS the creep damage in AISI 304 is reported in ref. [25]. Two AISI 304 specimens were submitted at creep at 600 °C with an applied stress of 176 MPa and at 550 °C with an applied stress of 211 MPa, respectively. The latter underwent fracture after 250 hours. The dependence of the microcavity volume fraction on the distance from the fracture was determined by SANS and is reported in Fig. 12.

The volume fraction C_c of the cavities was calculated by eq. 12, after $\widetilde{Q}_c$ (0) was extracted from the overall measured $\widetilde{Q}$ (0) by equation

$$\widetilde{Q}\ (0) = \widetilde{Q}\ (0)_c + \widetilde{Q}\ (0)_p \tag{16}$$

where $\widetilde{Q}(0)_p$ refers to the precipitate contribution.

Eq. 16 express the assumption that, for ageing times long enough, i.e. for saturation conditions, the volume fraction of the precipitates is independent from the applied stress, in spite of the fact that this one accelerates the growth of the precipitates. Under this assumption $\widetilde{Q}(0)_p$ was derived by the scattering cross section of a thermally treated sample for long time at the same temperature.

The cavity volume fraction so detected near the fracture surface $C_c = 2 \times 10^{-3}$ agrees perfectly [20] with the value estimated by a simple theoretical model [26]. The observed negative gradient of cavity volume fraction is to be related to a similar gradient observed for larger-size cavities by optical microscopy. Fig. 13 reports the cavity volume fraction as a function of the creep time for the first sample. Some simple theoretical considerations reported in ref. [25], suggest that the sample was in the stage of tertiary creep.

Fusion reactor materials

General considerations

As far as the confinement techniques of plasmas are obtaining substantial success, as the one recently obtained at JET, in U.K., and the construction of industrial prototypes is approaching in time, the development of materials suitable for facing the very severe conditions of operation becomes more and more urgent.

In particular in magnetic-confinement fusion reactors a critical component is the first wall, covering the internal surface of the reactor, directly exposed to thermomechanical perturbations and to irradiation of high-energy neutrons produced by the fusion reaction [20].

Precipitation in Al-Mg-Si

A SANS investigation of Mg_2Si precipitates in a single crystal of Al-Mg (0.72% wt)-Si (0.74% wt) alloy, which was considered as a possible candidate for the first wall of fusion reactors is reported in ref. [27]. Fig. 14a reports the experimental SANS anysotropic patterns obtained when the $<110>$ axis of the single crystal was parallel to the primary neutron beam direction after 24 hours ageing at 175 °C and 285 °C.

Fig. 14b reports the fitted scattering patterns obtained using the program based on spline functions reported in ref. [14].

The scattering precipitates were assumed to be of cylindrical shape growing preferentially along three orthogonal directions, having a length $L = 2kR$, R being the cylinder radius and k a geometrical factor to be determined by the best fit.

The fits of Fig. 14 were obtained for an orientation of the cylinder axis parallel to the three $<110>$ directions, for a value of $k = 8$ and for the radii distributions reported in Fig. 15. The size of the precipitates appear to increase by increasing the ageing temperature.

He bubbles in Ni

Neutrons trough (n, α) reactions lead to the production of He atoms and, trough diffusion processes, to He bubbles with a consequent damage of the material. At first study by SANS of He bubble formation and growth in Ni is reported in ref. [28] and [29].

SANS was able to detect a family of large diameter ($d \approx 10$ nm) He bubbles, which were at first not observed by TEM. Only after SANS measurements it was possible to discover by TEM, that in addition to a family of smaller bubbles in the bulk, a second family of larger bubbles was produced in surface and that there is a satisfactory agreement between the size distributions obtained by the two techniques.

He bubbles in MANET steel

Very recently a similar investigation was performed on Martensitic steel 1.4914 (or MANET), which constitutes a reference material for the class of low-activation martensitic alloys, which are possible candidates for the first wall. The interest of martensitic materials is the high level of nucleation which can occur not only at grain boundaries but also inside the grains, around the laths. The greater number of

bubbles implies smaller radii. This fact is an advantage because crack formation originates at helium bubble of larger radii and so the "helium embrittlement" is reduced in this case.

The first experiments [30] on MANET were able to show that SANS can distinguish between He-bubbles and precipitates, due to the different sizes of these two families of inhomogeneities. In fact Fig. 16a reports the size distributions of carbide precipitate in non-irradiated MANET as obtained by SANS and TEM and Fig. 16b the He bubble size distribution also obtained by the two techniques in α-irradiated samples after tempering at 800 °C for two hours.

Very recently α-irradiated MANET samples submitted to subsequent isochronal 2 hours annealing at 798, 948, 1098 and 1248 K were investigated by SANS [31]. Fig. 17a reports the scattering cross sections obtained for the reference and implanted samples after each common annealing step. It appears that only at 948 K a differentiation between the two cross sections is detected and is attributed to the He bubble formation. The corresponding He bubble size distributions obtained at 948, 1098 and 1248 K are reported in Fig. 17b. A progressive increase of the size is observed for increasing ageing temperatures.

Moreover, by using the data evaluation procedure described in [31] a quantitative estimation from the SANS data of the very high gas pressure in He bubbles was possible as a function of the bubble radius.

Metallic glasses

The thermal stability of amorphous metallic glasses can be investigated by SANS. Ref. [32] reports an investigation of amorphous Ti_{41} Zr_{41} Si_{18}. In asquenched samples SANS did detect the presence of inhomogeneitis of 8.1 nm radius, which disappeared during an annealing at 250 °C. This thermal treatment induced a structure relaxation toward a more stable non equilibrium state, which can be considered as an ideal amorphous. Moreover SANS was applied to investigate the complex microstructure evolution of samples annealed for different times at 500 °C.

Electronics materials

Small quantities (≈10 ppm) of dissolved oxygen are present in Czochralskigrown dislocation-free single crystals used for electronic devices production. This oxygen tends to segregate in cushion-shaped SiO_2 precipitates [33], which were investigated by SANS as a function of different parameters including the presence of boron. Fig. 18a reports the SANS pattern obtained for an undoped crystal treated at 1023 K for 24 h and at 1323 K for 20 h. A strong anisotropy is observed. Fig. 18b reports the corresponding simulation obtained by assuming SiO_2 precipitates of cuboid shape having dimensions $350 \times 350 \times 120$ $Å^3$. It is to emphasize the sensitivity of SANS in detecting inhomogeneities contained in very small volume fraction in this example.

Fig. 19 reports the measured (a) and calculated (b) isointensity lines for a fast neutron irradiated GaAs single crystal having the $<111>$ axis parallel to the incident beam [34]. The theoretical curves are obtained by assuming displacement cascades in form of ellipsoids elongated along [100] with an axial ratio $b/a = 5$.

Glasses

Several works were done on different types of glasses by SANS. Very recently a SANS study was

performed to study water condensation and freezing-defreezing process in porous Vycor glass [35].

Another recent SANS experiment was performed to study the microstructure in container glass in correlation with workability problems [36]. Bad workability [37] indicates sporadic cases in which the forming behaviour of industrially produced container glass undergoes variations without any apparent modification of the oxide composition, of the melting conditions or of the machine parameters. The origins of this effect are not well known and several hypoteses were made including microstructure formation.

In order to check this last point a first SANS experiment was performed on four ternary soda lime glass samples and four commercial soda lime silica glass samples. Fig. 20a reports the scattering cross section obtained for a model glass melted in the laboratory, then annealed, which appears transparent, with no sign of light scattering and supposed to be homogeneous. Fig. 20b reports the size distribution function obtained by the method reported in ref. [14].

Fig. 21a reports the scattering cross section obtained on the sample of Fig. 20 after a thermal treatment consisting in annealing, heat ageing for 1h at 600 °C and for 1h at 650 °C. This sample is bluish opalescent (Tyndall effect) with a high level of visible light scattering. Fig. 21b report the corresponding size distribution. It can be seen that the thermal treatment has induced a phase separation well "visible" by SANS.

Fig. 22a report the scattering cross section for one of the above mentioned commercial container glass samples, amber coloured, plant annealed and affected by low mechanical strength and Fig. 22b the scattering by the same sample for a thermal treatment of 6h at 630 °C. It appears that for both samples the scattering cross section versus Q is flat, that is there is no phase separation detectable. In fact the presence of inhomogeneities of dimensions lower than 1 nm cannot excluded, owing to the relative poor statistics. A future experiment with higher statistics should clarify this point.

Ref. [38] presents a review of X-ray and neutron SAS by mass-fractal silicas and porous glasses and calculations of the small-angle scattering from model fractal systems. Ref. [39] reports an investigation by SANS of microcrystallites in colored glasses and ref. [40] a study of the structural and dynamical properties of superionic conductor glasses.

Recently a SANS investigation [41] was performed on phase separation in glasses of the systems Na_2O-CaO-SiO_2, Na_2O-Al_2O_3-B_2O_3-SiO_2 and MgO-Al_2O_3-SiO_2. In particular it was discovered, by using the method of contrast variation, that the TiO_2 additive is inhomogeneously distributed in phase separated MgO-Al_2O_3-SiO_2 base glasses for glass ceramics, accumulating at the interface particle-matrix.

High T_c Superconductors

In order to understand the basic aspects and application involments of the phenomena associated to superconductivity in compounds which exhibit high temperature transition, it is important to have more information about their structural properties and in particular about defects. SANS was applied to investigate the microstructure [42] of Y Ba_2 Cu_3 O_6 and Y Ba_2 Cu_3 $O_{6.9}$.

Fig. 23 reports the 3 dimensional representation of SANS intensity pattern of the Y Ba_2 Cu_3 O_6 compound. The scattering appears to be highly anisotropic and is attributed to platelet-shaped particles with large dimensions (>0.5 μm) perpendicular to the z axis and 100 Å thickness.

The nature of these particles could be associated to clustering of impurities or partial fluctuations of one atomic species (for istance Cu) or to magnetic contribution with correlated dynamical fluctuations.

Ceramics

SANS technique can find useful application in the investigation of structural properties of ceramics, apart from the high T_c superconductors. A recent experiment [43] did investigate the evolution of the pore microstructure of glassy silica and polycrystalline alpha-alumina as a function of syntering mechanism.

Catalysts

Some samples of the Vanadium-Tinanium oxide catalyst, obtained both by laser-induced process (pure TiO_2 and $Ti_{1-X}\ V_XO_2$) and by chemical impregnation of TiO_2 with V_2O_5 were investigated by SANS as cast and calcined for different times [44].

Fibres

A SANS experiment was performed on porous alumina fibres [45]. An anisotropic scattering was observed from bundles of 3 μm diameter fibres and was interpreted by assuming three different contributions to the scattering, namely the fibres themselves, randomly oriented pores, and oriented pores, for which quantitative structural imformation was obtained. Moreover ref. [46] reports a structural investigation by SANS of carbon fibres, used in the production of composite materials.

Composites

SANS can be useful to investigate the microstructural parameters associated to composites. An example of this kind of investigation on aluminium based composites in comparison with the unreinforced alloy can be found in ref. [47].

Cements clays and porous rocks

Ref. [48] presents a review of the applications of SANS for the microstructural characterization of scale-invariant (fractal) disordered materials like cements, clays and porous rocks.

Miscellanea

Several other interesting microstructural investigations by SANS on different materials were performed and will be briefly mentioned here. In ref. [49] the growth rates of grain boundary cavities during high temperature fatigue of copper was investigated. The volume fraction of cavities was obtained by using an Archimedes balance. Then the cavity specific surface was obtained from the SANS data by using the Porod analysis (see section 2.3.3). By assuming that all the cavities have the same volume, the radius of each cavity was then obtained by combining the two quantities, and as a consequence also the number of cavities. Fig. 24 reports some data obtained in this experiment, namely the volume of each cavity and the number of cavities as a function of the number of cycles.

A more sophisticated experiment of this kind is reported in ref. [50], where the void size and dislocation density were determined as a function of fatigue cycles in a Cu single crystal. Furthermore SANS was recently used to investigate the microstructure of nanocrystals. In particular ref. [51] reports a study on nanocrystalline TiO_2 and Ni at different degrees of compactness.

Conclusions

We hope that the several reported examples of applications of Small Angle Neutron Scattering to a variety of material, is sufficient to show that this technique becomes day by day more and more useful in solving structural problems not only in classical scientific field, but also in interdisciplinary subjects and in several technological areas.

Acknowledgements

It is a pleasure to thank Miss Simona Franguelli for typing the manuscript and Mr. Sirio Polenta for the drawings preparations.

References

[1] Proc. of Int. School of Physics "Enrico Fermi", Course CXIV, *Industrial and Technological Applications of Neutrons*, Lerici, June 19-29 (1990). M. Fontana, F. Rustichelli and R. Coppola Eds., North Holland (1992).
[2] Bacon, G.E. Neutron Diffraction. Oxford University Press, London and New York, (1981).
[3] Guinier, A., and G. Fournet. Small Angle Scattering of X-rays. John Wiley (Ed.), New York, (1955).
[4] Guinier, A. X-Ray Diffraction. Freeman (Ed.), San Francisco, (1963).
[5] Beeman, W.W., P. Kaesberg, J.W. Anderegg, and M.B. Webb. In S. Flugge (Ed.) Handbuch der Physik, Springer-Verlag, Berlin and New York, (1957), vol. 32, p. 321.
[6] Walther, H., and A. Pizzi, *Small Angle Neutron Scattering*. In R.S. Sharpe (Ed.), *Research Techniques in Nondestructive Testing*, Academic Press, New York, (1980), p. 341.
[7] Kostorz, G., *Small Angle Scattering and its applications to material sciences*. In G. Kostorz (Ed.), *Neutron Scattering*, Academic Press, New York, (1979), vol. 15, p. 227.
[8] Kostorz, G., in Physical Metallurgy, 3 rd ed., edited by R.W. Cahn and P. Haasen (North-Holland, Amsterdam, 1983), p. 793.
[9] Guinier, A., Solid State Phys., 9 (1959), 294.
[10] Schmatz, W., T. Springer, J. Schelten, and K. Ibel. J. Appl. Crystallogr., 7 (1974), 96.
[11] Kostorz, G., Proc. of Int. School of Physics "Enrico Fermi", Course CXIV, *Industrial and Technological Applications of Neutrons* (Lerici, June 19-29, 1990) M. Fontana, F. Rustichelli and R. Coppola Eds, North Holland (1992) p. 85.
[12] Porod, G. Acta Phys. Austriaca, 2 (1948), 255.
[13] Fedorova, I.S. and P. W Schmidt. J. Appl. Cryst. 11 (1978) p. 405.
[14] Magnani, M., P. Puliti, M. Stefanon. Nucl. Instr. Methods Phys. Res. Sect. A, 271 (1988), 611 and references therein.
[15] Abis, S., R. Caciuffo, F. Carsughi, R. Coppola, M. Magnani, F. Rustichelli, M. Stefanon, Phys. Rev. B42 (1990), 2275.
[16] Ibel, K., J. Appl. Crystallogr., 9 (1976) 296.
[17] Kulda, J., and P. Mikula, J. Appl. Crystallogr., 16 (1983) 498.
[18] Galotto, C.P., P. Pizzi, H. Walther, V. Angelastro, N. Cerullo, G. Cherubini, Nucl. Instr. and Methods, 134 (1976) 369.
[19] Bellet, D., P. Bastie, A. Royer, J. Lajzerowicz, J.F. Legrand, R. Bonnet, J. de Physique, J. Phys. I France 2 (1992) 1097.

[20] Albertini, G., F. Carsughi, R. Coppola, D. D'Angelo, Proc. of Int. School of Physics "Enrico Fermi" Course CXIV, *Industrial and Technological Applications of Neutrons* (Lerici, June 19-29, 1990) M. Fontana, F. Rustichelli and R. Coppola Eds, North Holland (1992) p. 145.
[21] Bianchi, P., F. Carsughi, D. D'Angelo, M. Magnani, M. Stefanon, F. Rustichelli, Metall. Sci. Technol. 6 (1988) 13.
[22] Bianchi, P., F. Carsughi, D. D'Angelo, J. Kulda, A. Mengoni, P. Mikula, F. Rustichelli, Mater. Sci. Forum 27/28 (1988) 429.
[23] Bianchi, P., F. Carsughi, D. D'Angelo, M. Magnani, A. Olchini, M. Stefanon, F. Rustichelli, Physica B, 156/157 (1989) 688 and Superalloys 1988 (Ed. S. Reichman, D.N. Duhl, G. Maurer, S. Antolovitch, C. Lund) The Metallurgical Society (1988) p. 845.
[24] Boeuf, A., R. Coppola, S. Maggi, S. Melone, P. Puliti, F. Rustichelli, F. Zambonardi, J. Appl. Crystallogr., 14 (1981) 337.
[25] Boeuf, A., R. Coppola, F. Rustichelli, F. Zambonardi, S. Melone, P. Puliti, in Proceedings of Joint Conference JRC (Ispra). Metal Society (London) (Metal Society, London 1982 p. 94).
[26] Caglioti, G., Mater. Science Eng. 28 (1976) 153.
[27] S. Abis, R. Caciuffo, R. Coppola, P. Fiorini, M. Magnani, F. Rustichelli, M. Stefanon, Mat. Sc. Forum 13/14 (1987) 295.
[28] Schwahn, D., H. Ullmaier, J. Schelten, W. Kesternich, Acta Met. 31 (1983) 2003.
[29] Kesternich, W., D. Schwahn, H. Ullmaier, Scripta Metallurgica 18 (1984) 1011.
[30] Albertini, G., F. Carsughi, R. Coppola, F. Rustichelli, W.A.H.M. Vlak, C. Van Dijk, J. Nucl. Mat., 179 (1991) 706 and G. Albertini, F. Carsughi, R. Coppola, F. Rustichelli, D. Schwahn, G. Mercurio, Nuclear Instruments and Methods A321 (1992) 381.
[31] Albertini, G., F. Carsughi, R. Coppola, W. Kesternich, G. Mercurio, F. Rustichelli, D. Schwahn, H. Ullmaier, J. Nucl. Mat., in print.
[32] Bordely, S., L.S. Smirniv, Yu. K. Kovneristii, T.T. Nartova, O.B. Tarasova, V.Yu Berzabotnov, Yu. M. Ostanevich, Phys. Stat Sol. (b) 164 (1991) 343.
[33] Gupta, S., S. Messoloras, J.R. Schmeder, R.J. Stewart, W. Zulehnder, J. Appl. Cryst. 24 (1991) 576.
[34] Gupta, S., Ph. D. Thesis, University of Reading (1976).
[35] Li, J.C., D.K. Ross, M.J. Benham, J. Appl. Cryst., 24 (1991) 794.
[36] Albertini, G., A. Benedetti, F. Carsughi, M.M. De Morais, O. Francescangeli, F. Geotti-Bianchini, F. Rustichelli, M. Stefanon, Materials Science and Engineering, A161 (1993) 157.
[37] Poole, J.P., Proceed of XI Int. Congr. Glass, Prague 1977, P. 307; Geotti-Bianchini, F., Glastech. Ber. 65 (1992) 306; 329.
[38] Schmidt. P.W., J. Appl. Cryst., 24 (1991) 414.
[39] Bangi, G.P., V. Degiorgio, *Proceeding of the SPIE* - The Intern. Soc. for Optical Eng. 1361 Pt. 2 (1991) 874.
[40] Dianoux, A.J., M. Tachez, P. Mercier, I.P. Malugani, J. of Non - Crystalline Solids 130 (1991) 973.
[41] Lembke, U., A. Hoell, R. Kranold, R. Brueckner, IX International Conference on Small Angle Scattering, Saclay 27-30 April 1993.
[42] Kahn, R., A. Brulet, G. Collin, B. Farnoux, Physica C 159 (1989) 323.
[43] Long, G.G., S. Krueger, R.A. Gerhardt, R.A. Page, J. of Mat. Res. 6 (1991) 2706.
[44] Albertini, G., F. Carsughi, C. Casale, F. Fiori, A. La Monaca, M. Musci, in print.
[45] Jones, A.F., I.B. Parker, M.H. Stacey, J. Appl. Cryst., 24 (1991) 607.
[46] Sizov, R.A., G.V. Neiman, M. Yu. Digilov, O.T. Malyuchkov, Inorganic Materials, 25 (1989) 684.
[47] Salvo, L., C. Servant, M. Suéry, IX International Conference on Small Angle Scattering, Saclay 27-30 April 1993.
[48] Allen, A.J., J. Appl. Cryst., 24 (1991) 624.
[49] Barker, J.G., J.R. Weertman, Scripta Metallurgica et Materalia 24 (1990) 227.
[50] Lepisto, T.K., G. Kostorz, V.T. Knokkala, P. Kettunen, Mat. Sci. and Engn. A131 (1991) 171.
[51] Muller-Stach, M., H. Franz, U. Herr, J. Peisl, W. Petry, G. Wallner, J. Appl. Cryst. 24 (1991) 603.
[52] Albertini, G., P. Bianchi, F. Carsughi, D. D'Angelo, F. Rustichelli, M. Stefanon, to be published.

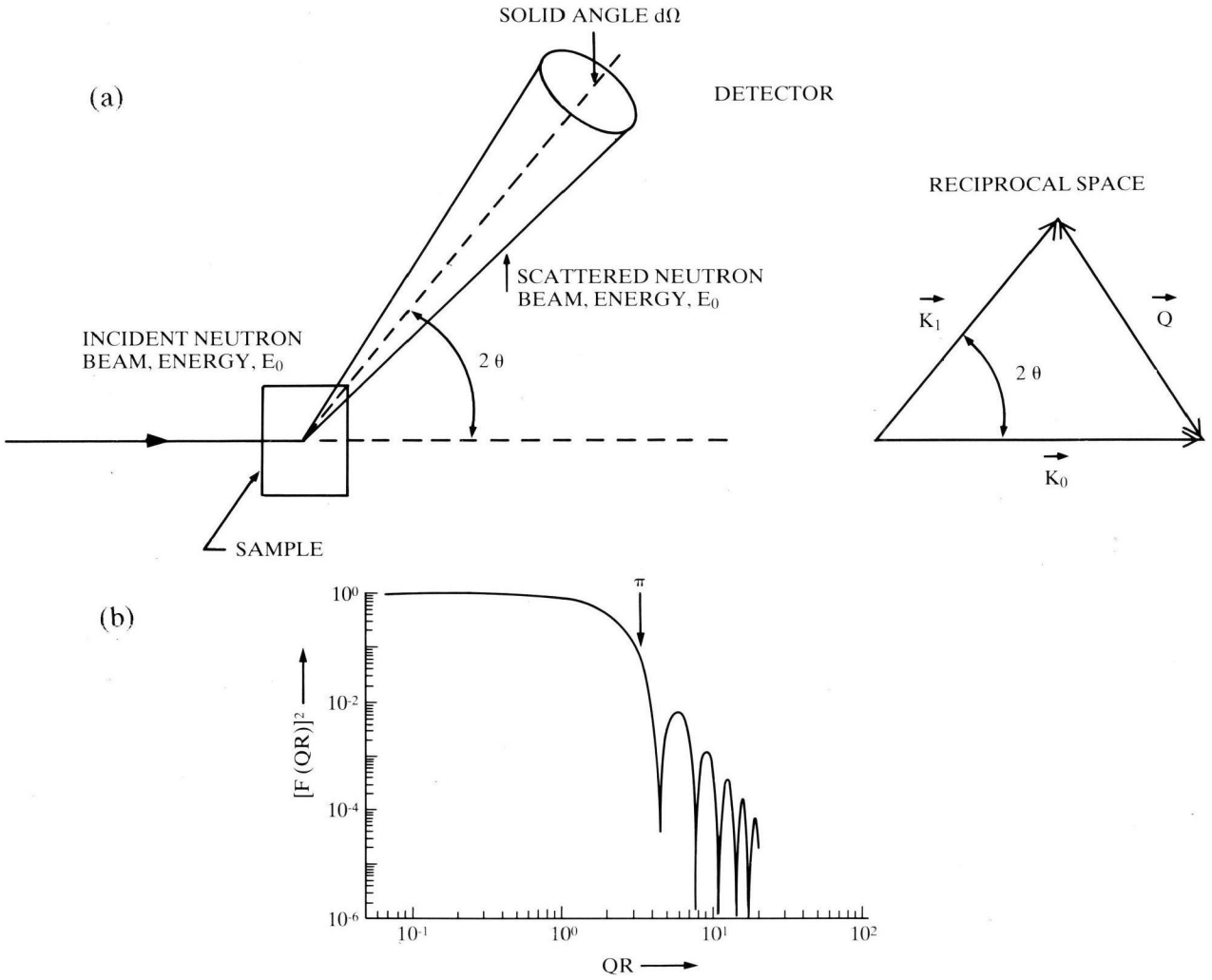

Fig. 1:
(a) Schematic representation of the coherent elastic process in real space and the reciprocal space; (b) scattering function of a sphere of radiud R.

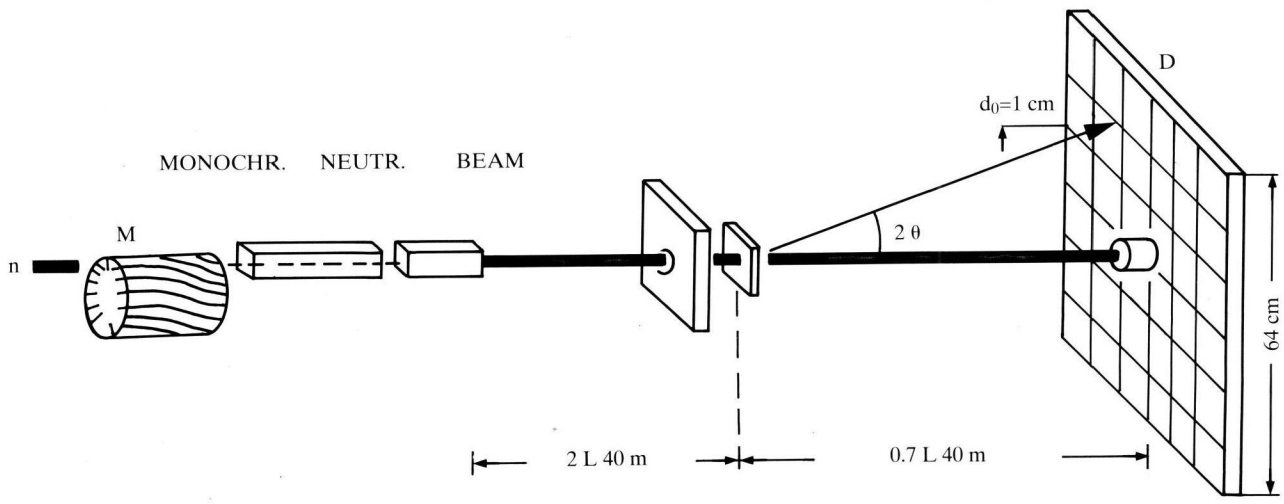

Fig. 2:
The D11 SANS diffractometer installed at the High Flux reactor at ILL Grenoble.

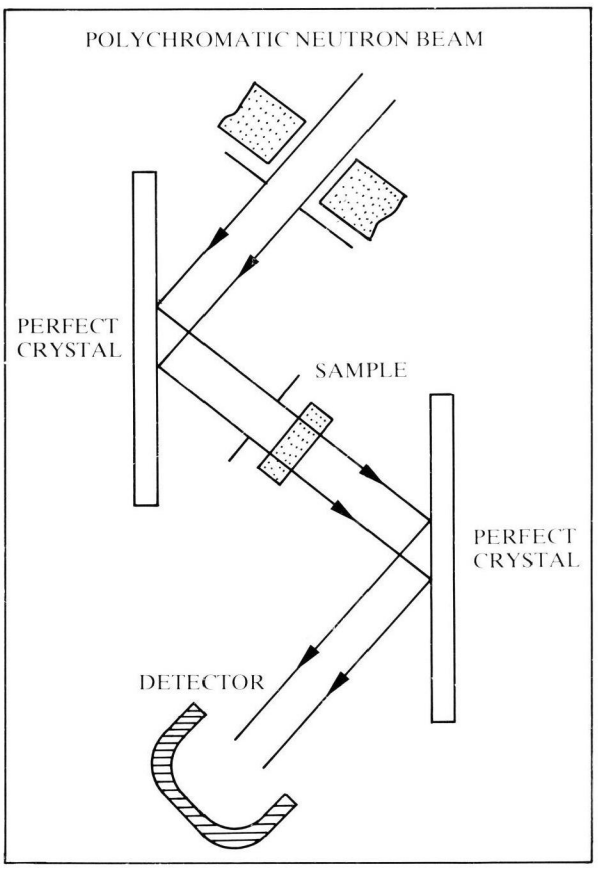

Fig. 3:
Schematic representation of a very high resolution double crystal SANS diffractometer.

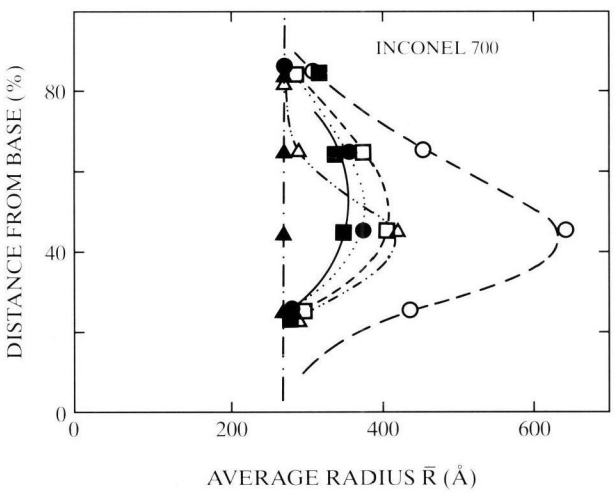

Fig. 4:
Average radius of γ′ precipitates in INCONEL 700 turbine blades operated for different times under normal (▲: Ohr; ●: 274hr; ■: 394hr; □: 912hr) and elevated (△: 51hr; ○: 395hr) temperature conditions [18].

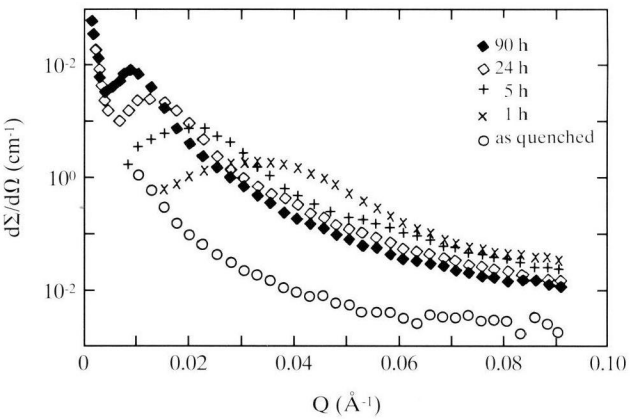

Fig. 5:
SANS cross sections measured for Al-Li (3 wt.%) samples aged at 463 K for various amounts of time. Spatial correlation between the precipitates is revealed by the presence of a diffuse interference peak [15].

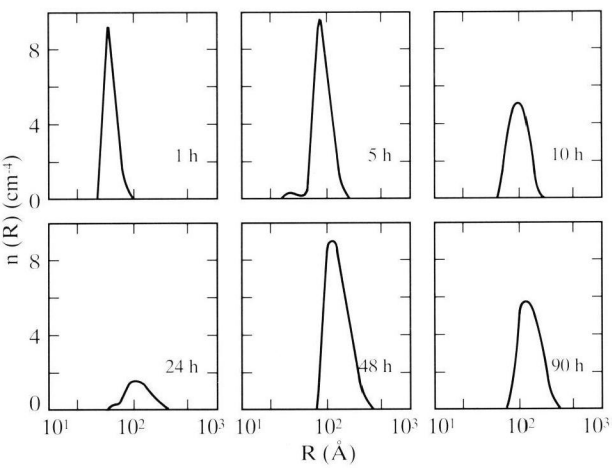

Fig. 6:
Distribution of δ′ particle sizes in Al-Li (3 wt.%) samples aged at 463 K for different amounts of time; n(R) dR represents the number of particles per unit volume with radius between R and R + dR. The calculated errors are indicated by bars. Note the change of scale on the y axis [15].

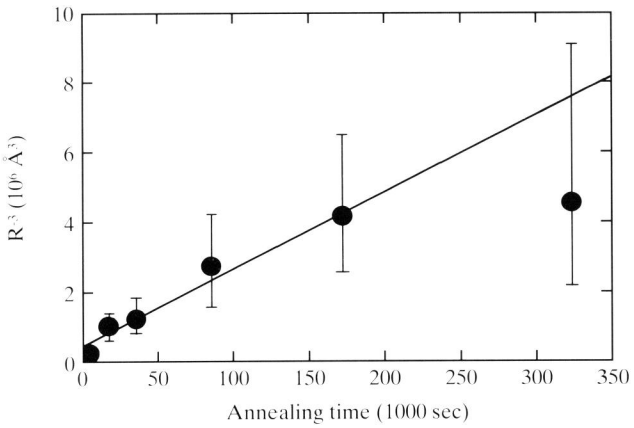

Fig. 7:
The cube of the average radius of the δ′ precipitates vs the ageing time. A linear relation holds, in agreement with the predictions of diffusion-controlled coarsening models. A growth rate K = 22 Å^3/s is found. The vertical bar represents the root-mean-square width of the N(R) distribution [15].

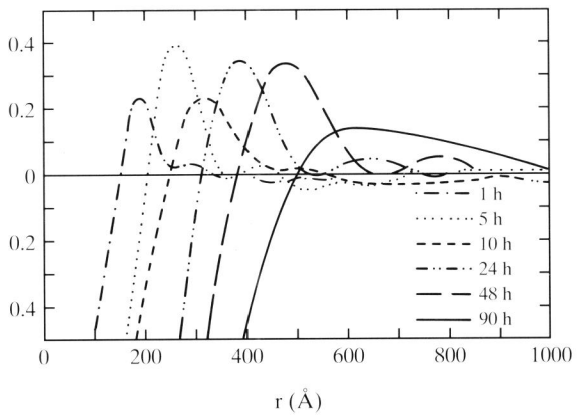

Fig. 8:
Effective reduced pair correlation functions $g_e(r)$ for δ′ precipitates in the investigated alloy. The position of the maximum gives the radius of the first coordination shell [15].

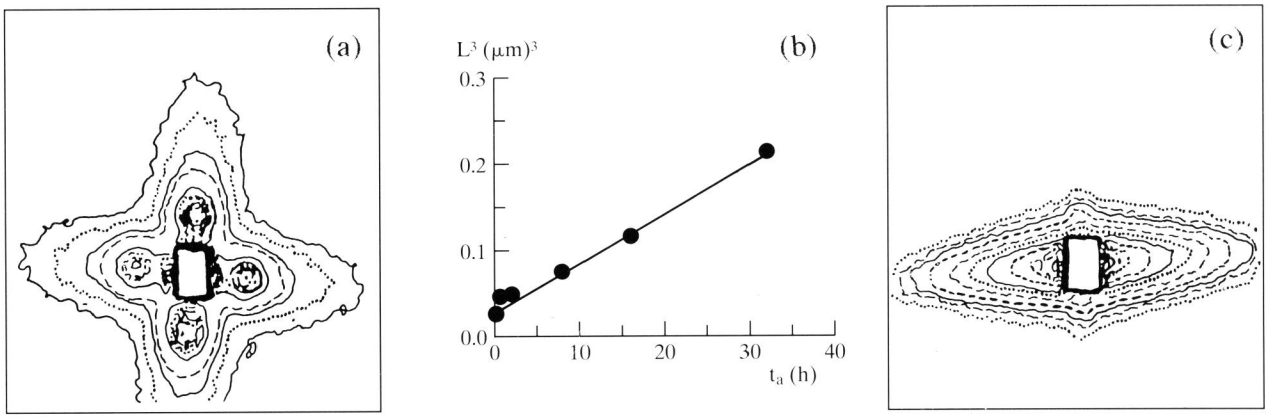

Fig. 9:
(a) SANS iso-intensity contours of AM1 superalloy annealed 2 hours at 1050 °C, (001) plane.
(b) Dependence of the γ′ precipitate volume L^3 on the annealing time at 1050 °C.
(c) SANS iso-intensity contours of AM1 superalloy crept at 950 °C, σ = 280 MPa, ε = 1.5% along <001> direction, (010), plane [19].

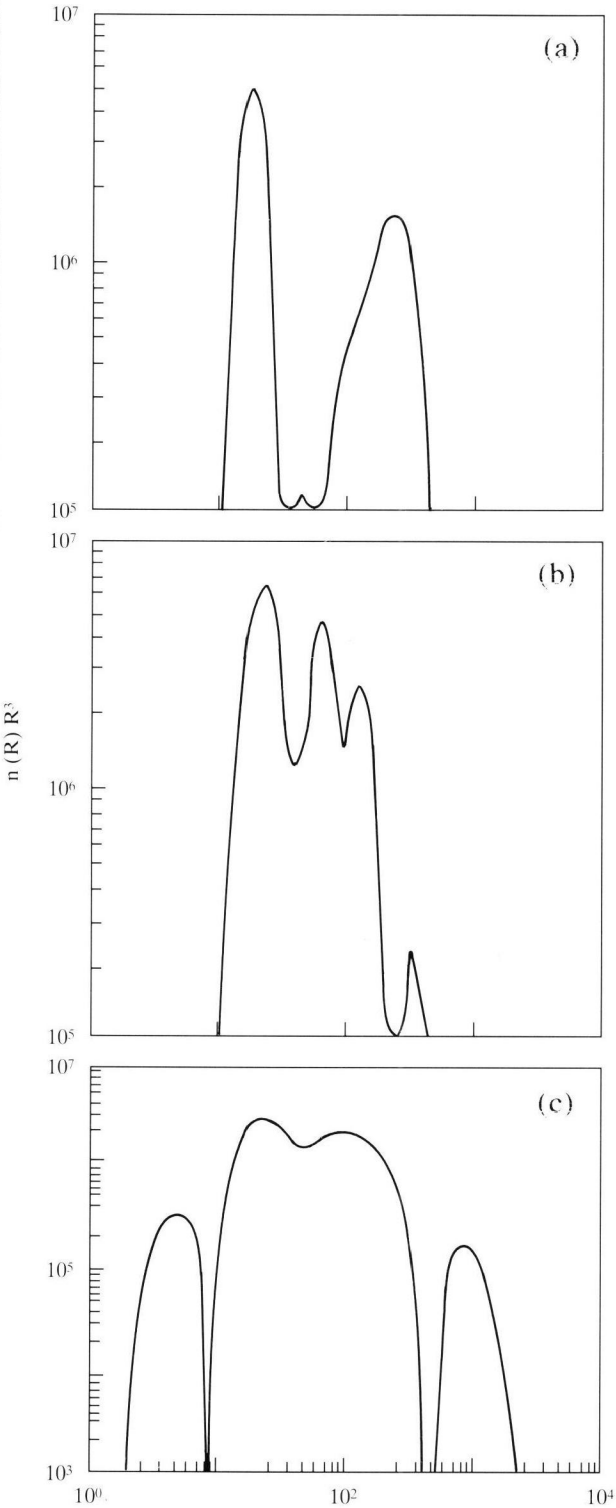

Fig. 10:
Size distribution of γ′ precipitates in UDIMET 720 superalloy non treated material (a); in a turbine blade before operation (b); and after 8000 h operation at 800 °C (c) [21] [23].

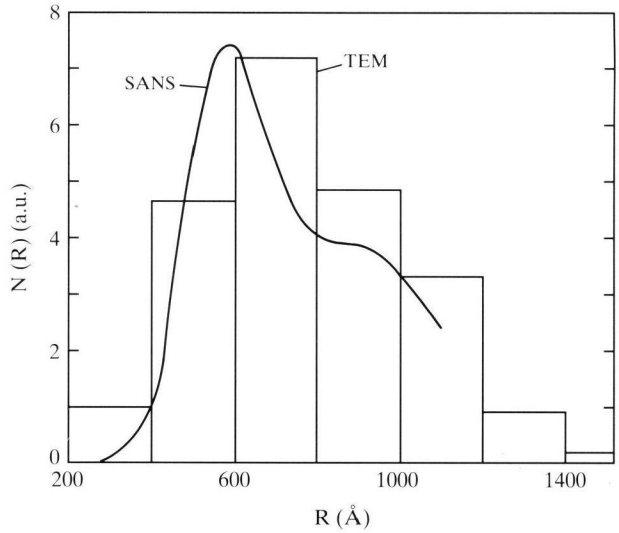

Fig. 11:
Size distribution from SANS of $M_{23}C_6$ (carbide) precipitates in AISI 304 stainless steel aged at 700 °C for 60 days, in comparison with transmission electron microscopy hystogram [24].

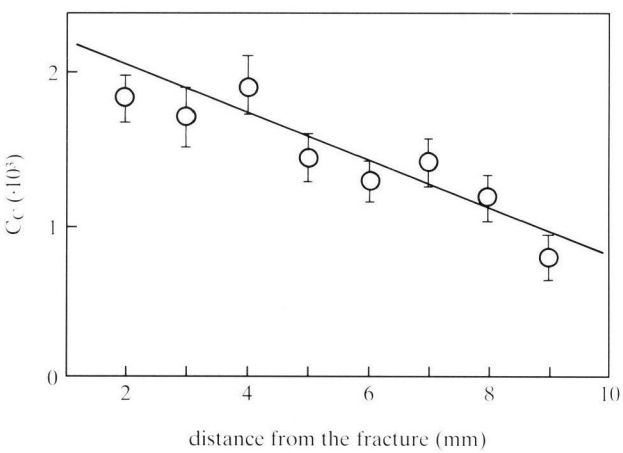

Fig. 12:
Volume fraction of cavities C_c along a fractured sample of AISI 304 stainles steel submitted to creep treatment under a stress of 211 MPa at 550 °C for 250 h [25].

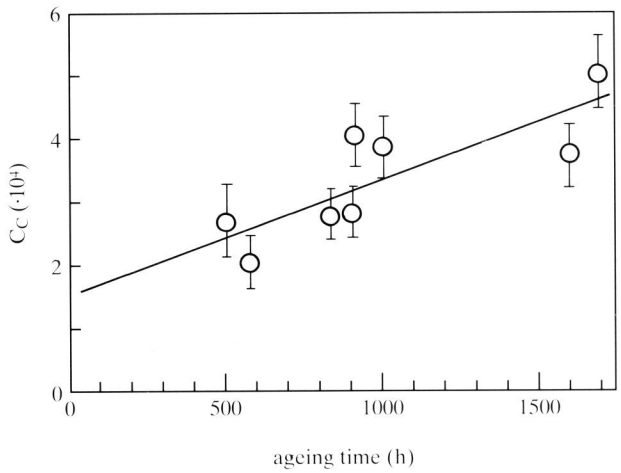

Fig. 13:
Volume fraction of cavities C_c as a function of treatment time for samples creep-tested at 600 °C under a stress of 176 MPa [25].

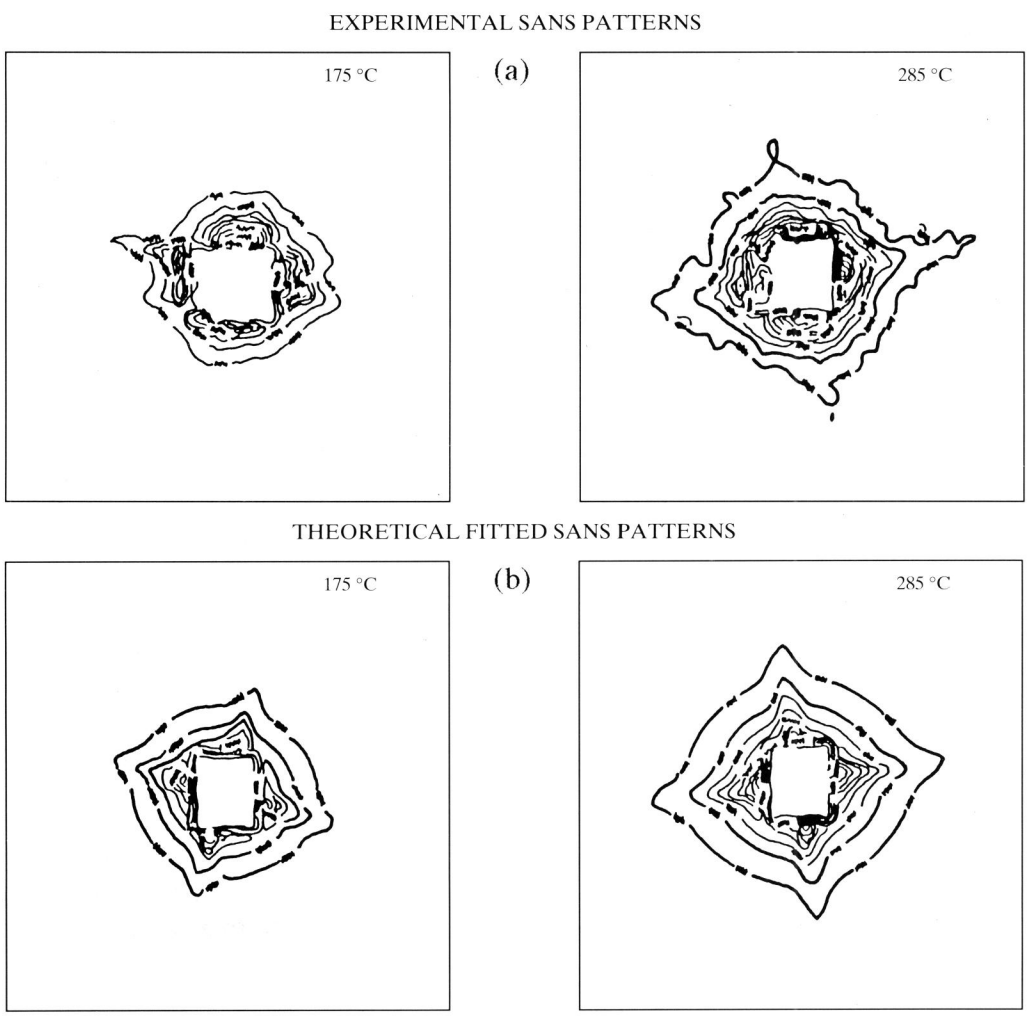

Fig. 14:
(a) Experimental SANS pattern from a single crystal of Al-Mg (0.72% wt)-Si (0.74% wt) alloy, aged for 24 hours at 175 °C and 285 °C, the <110> axis being parallel to the primary neutron beam direction; (b) theoretical SANS fitted pattern: the corresponding precipitate size distribution are reported in fig. 15 [27].

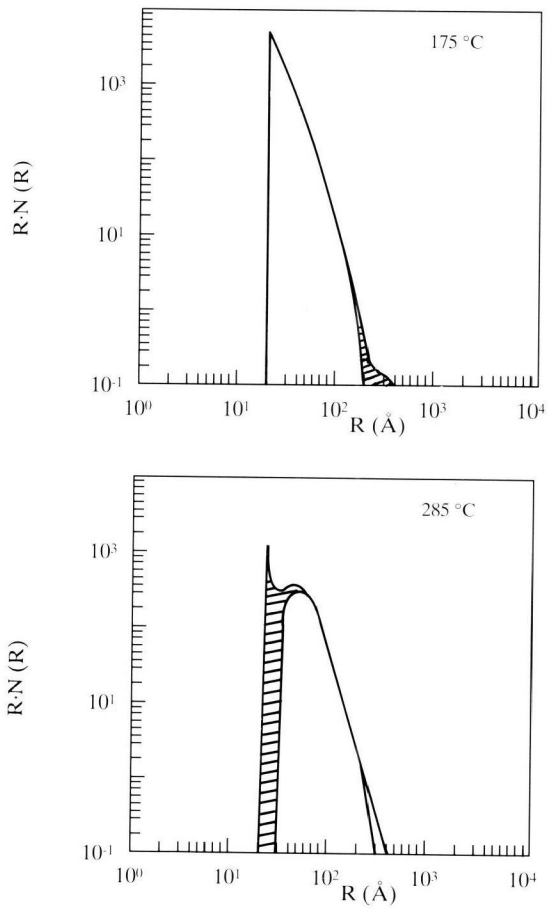

Fig. 15:
Mg_2Si precipitate size distribution deduced from the data of Fig. 14 [27].

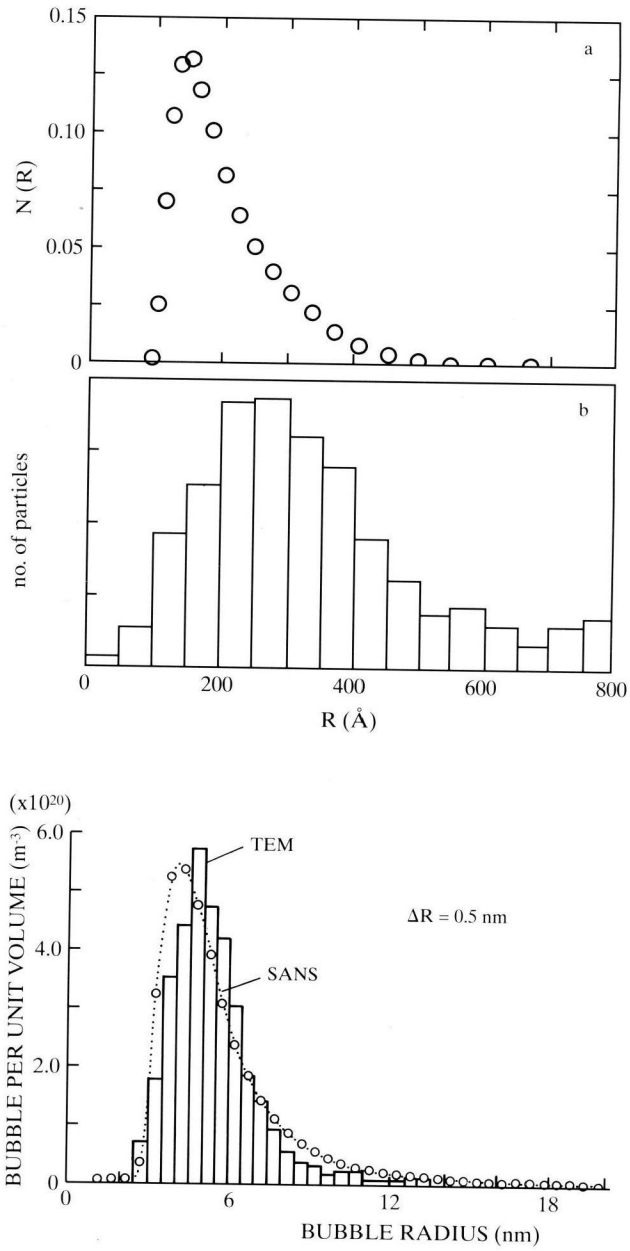

Fig. 16:
(a) Size distribution of $M_{23}C_6$ (carbide) precipitate in non-irradiated MANET steel as obtained by SANS and TEM;
(b) size distribution of He bubbles in α-irradiated samples of MANET after tempering at 800 °C for two hours [30].

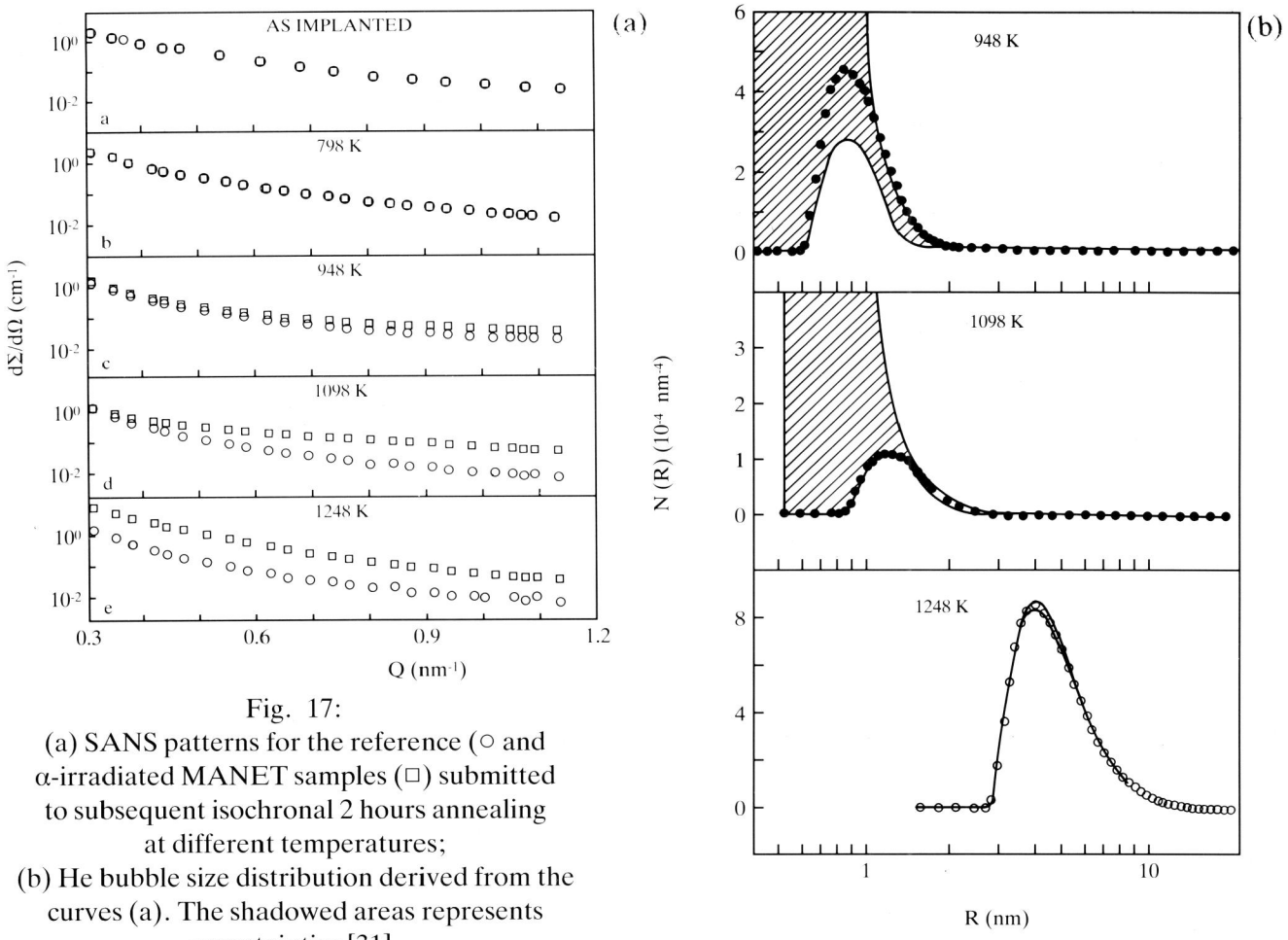

Fig. 17:
(a) SANS patterns for the reference (○ and α-irradiated MANET samples (□) submitted to subsequent isochronal 2 hours annealing at different temperatures;
(b) He bubble size distribution derived from the curves (a). The shadowed areas represents uncertainties [31].

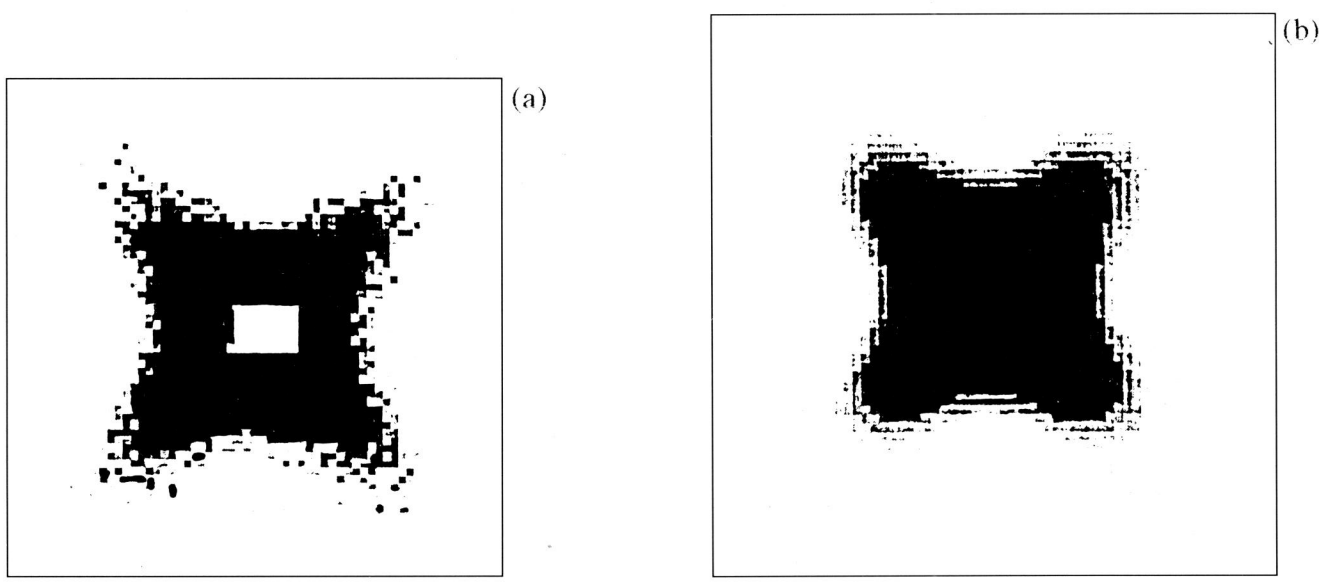

Fig. 18:
(a) SANS patterns for a Si single crystal treated at 1023 K for 24 hours and at 1323 K for 20 hours;
(b) simulation of the pattern (a) by assuming SiO_2 precipitates of cuboid shape $350 \times 350 \times 120$ Å^3 [33].

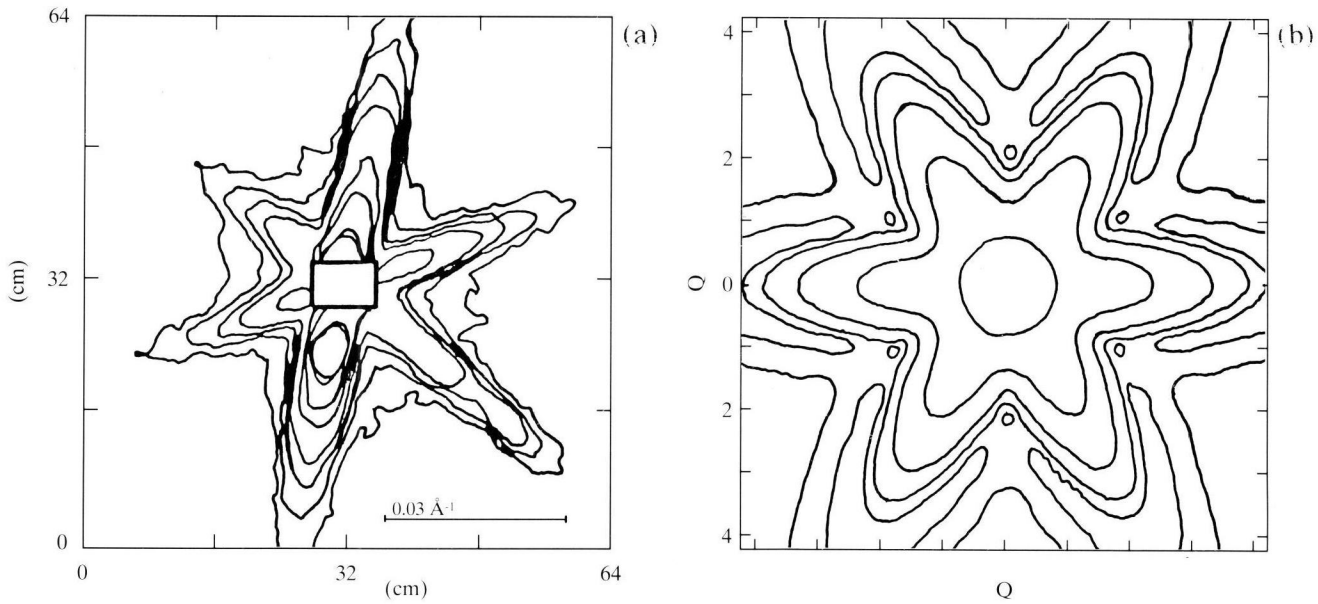

Fig. 19:
(a) SANS isointensity contours for a fast neutron irradiated GaAs single crystal having the <111> axis parallel to the incident beam; (b) simulation of the pattern (a) by assuming displacement cascades in form of ellipsoids elongated along [100] with an axial ratio b/a = 5 [34].

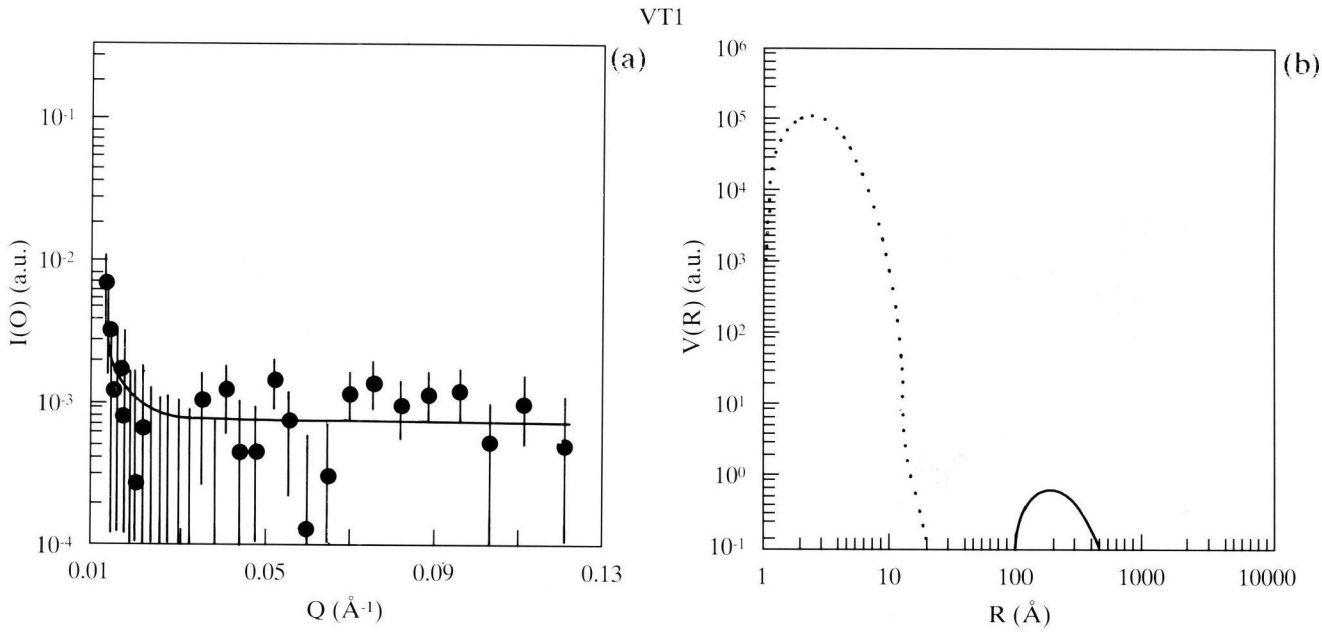

Fig. 20:
(a) SANS pattern for a model glass, melted and then annealed;
(b) size distribution of inhomogeneities [36].

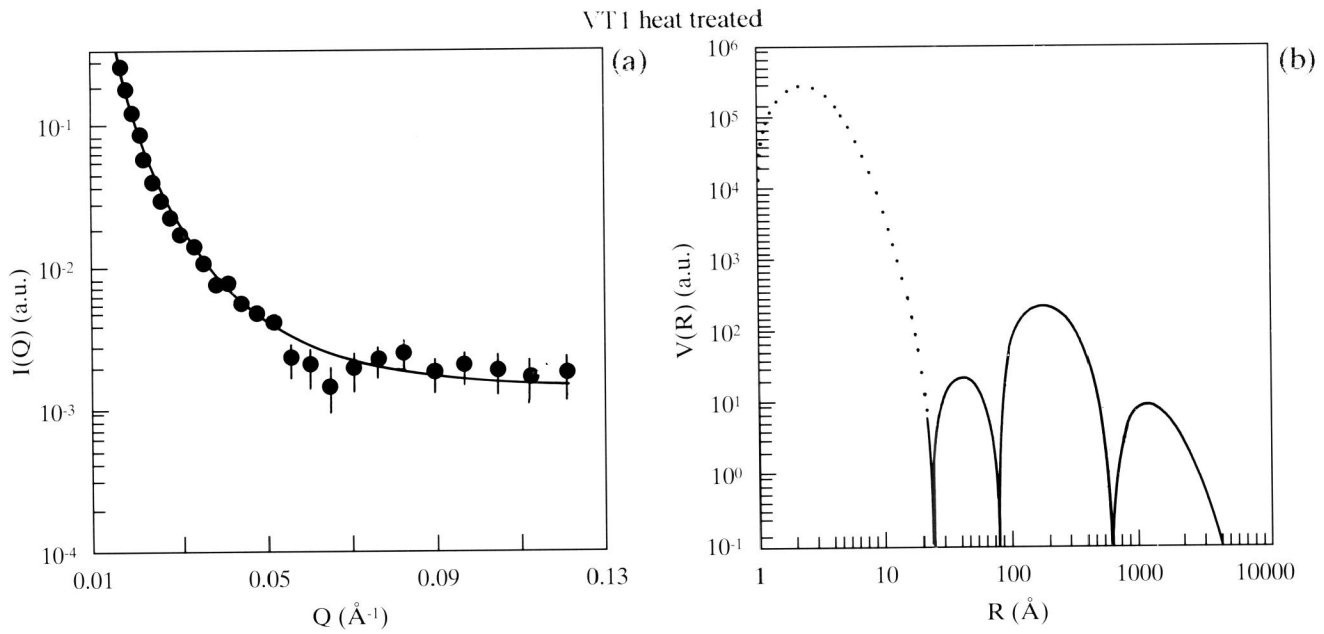

Fig. 21:
(a) SANS of the model glass after annealing, heat ageing for 1 hour at 600 °C and for 1 hour at 650 °C;
(b) size distribution of inhomogeneities [36].

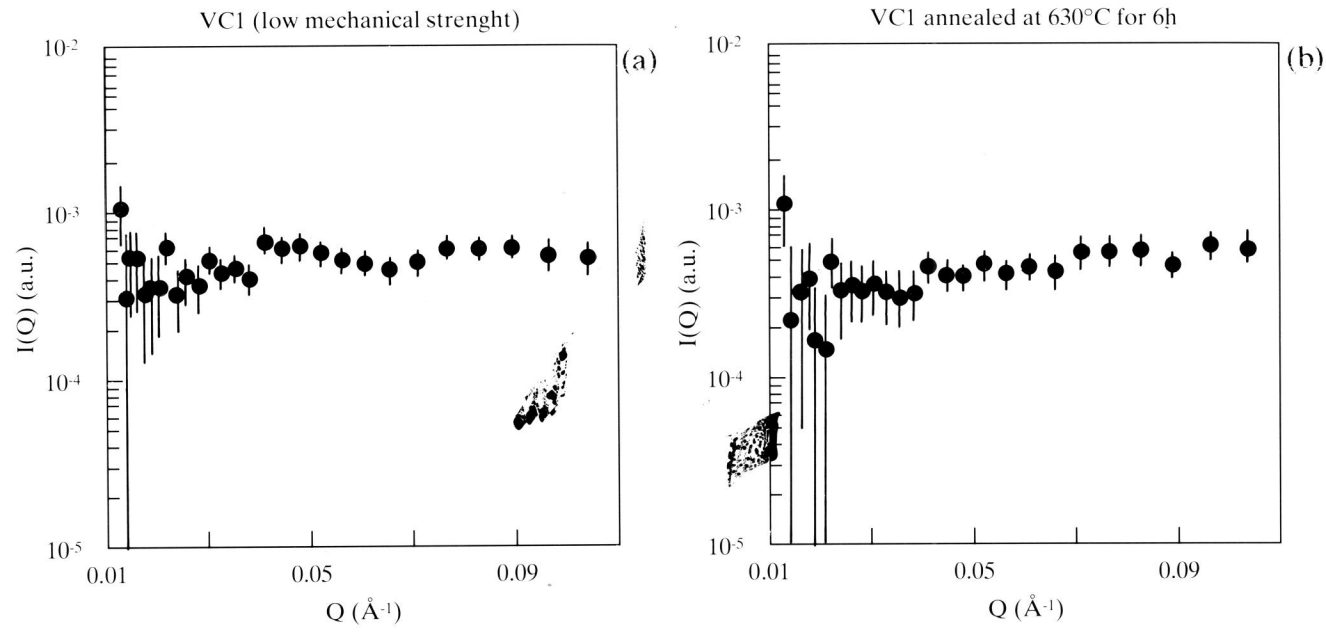

Fig. 22:
(a) SANS of a commercial glass; (b) SANS of the same sample after annealing and heat ageing for 6 hours at 630 °C [36].

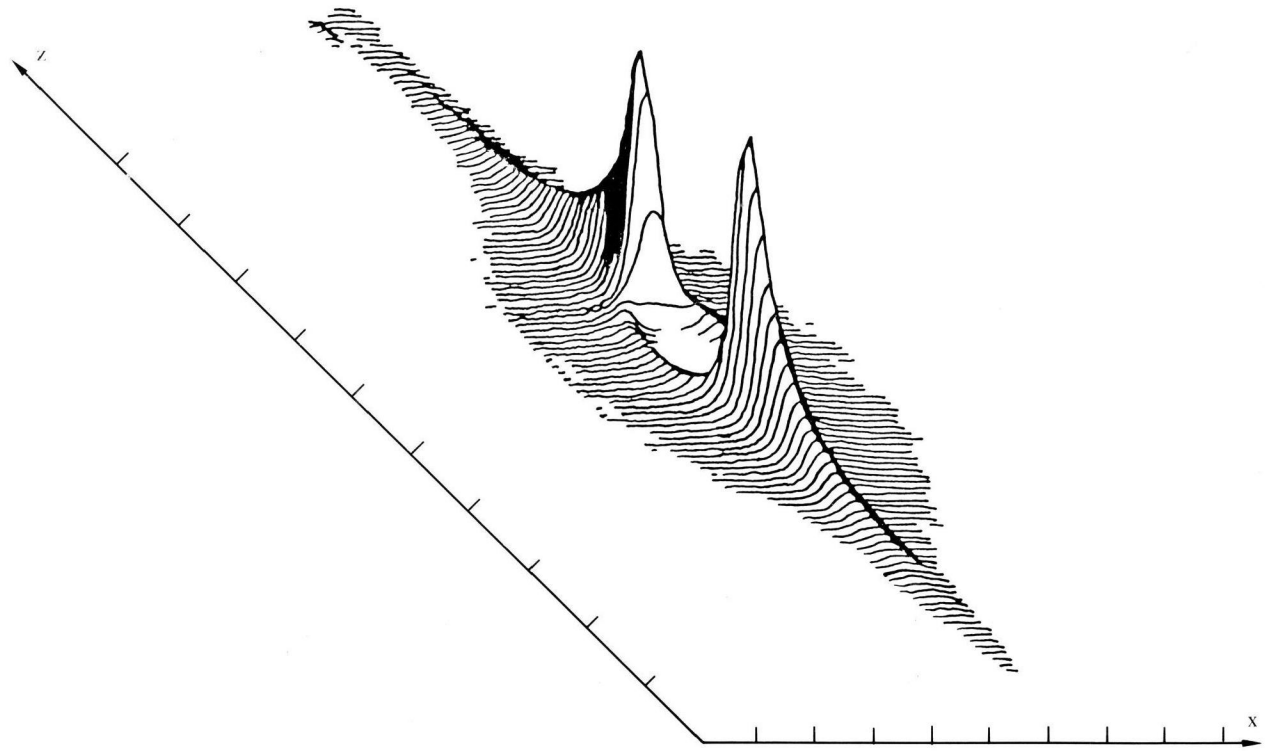

Fig. 23:
SANS pattern of $YBa_2Cu_3O_6$ high T_c superconductor [42]. The hollow in the center is due to the beam stop.

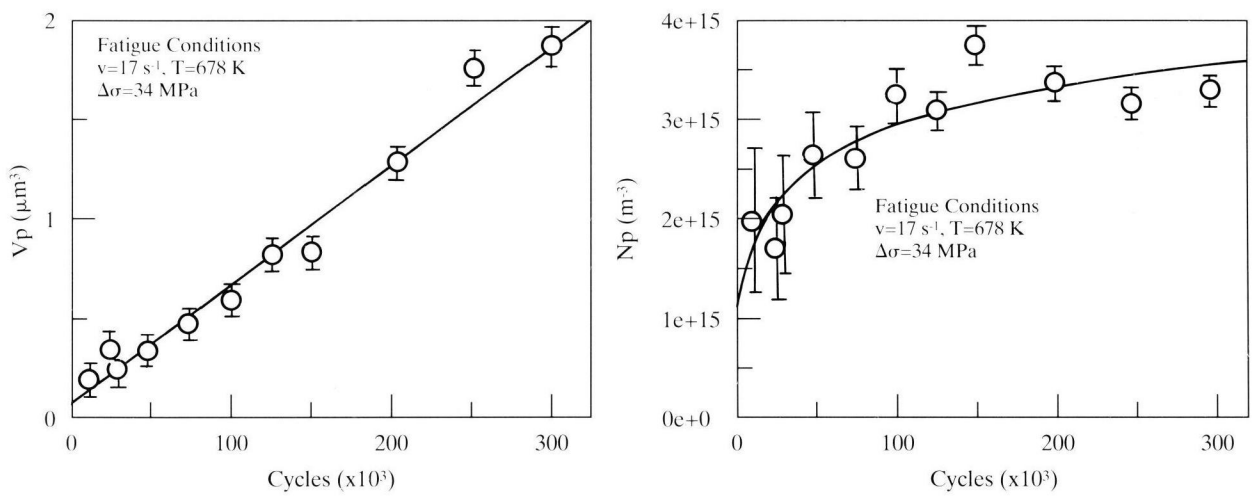

Fig. 24:
The volume of each cavity and the number of cavities as a function of the number of cycles, in high temperature fatigue of Cu [49].